Discrete-Time Nonlinear Control Technique for Trajectory Tracking of Hybrid Reluctance Actuator

M. R. Homaeinezhad[1*], M. M. Ebrahimi[1], M. M. Mousavi Alvar[1]

[1]Faculty of Mechanical Engineering, K. N. Toosi University of Technology, Tehran, Iran

*** Corresponding Author:** M. R. Homaeinezhad
Faculty of Mechanical Engineering, K. N. Toosi University of Technology, No. 17, Pardis Street, Mollasadra Ave., Vanak Square, Tehran, Iran. **P.O Box:** 19395-1999, **Postal Code:** 19991-43344.
Tel: (+98 21) 84063284**, Mobile:** (+98) 9121899445**, Fax:** (+98 21) 88677274.
Emails: mrhomaeinezhad@kntu.ac.ir; mrh.kntu@gmail.com

Abstract

Electromagnetic actuators are highly effective for manipulating flexible nanoscale objects, with Hybrid Reluctance Actuators (HRA) being a notable type. HRAs feature an iron core with an embedded magnet to strengthen the magnetic field. By adjusting the flux in the yoke using coil wires, HRAs can apply precise forces to the driven component. This paper formulates the HRA circuit model, incorporating structural uncertainties and nonlinear state-space equations. The key distinction of this system is the combination of nonlinear inputs with state variables. A model-based dual-mode control algorithm is developed for effective HRA control, employing power reaching laws for position and velocity control to ensure stability and accuracy. The actuator system faces constraints, leading to saturation limitations on electromagnetic force. This work innovatively includes actuator constraints in control law extraction, enabling the system to track a modified desired trajectory. A one-step predicting cost function for mode selection is defined, allowing the controller with the smaller cost function to be chosen. An adaptive lookup table is used to manage the complex direct dynamics, updated at each time step to link control input and electromagnetic force. MATLAB simulations confirm the control algorithm's performance, achieving 2 nm precision within saturation limits.

Key words: Nanometric Positioning; Electromagnetic Actuator; Hybrid Reluctance Actuator; Nanoscale Control; Saturation; Hybrid Mode Control; Nonlinear Actuation Mapping

1. Introduction

Electromagnetic positioners, essential in nanoscale control, find applications in nanotechnology, materials science, microscopy, and precision instrumentation [1–4],.[5] They enable sub-nanometer accuracy through mechanisms like piezoelectric nano-positioners [6,7], [8], [9]. Electromagnetic positioners [10–12] offer high force for special scanning systems and force-based microscopy, as documented in the same reference, while flexure-based nano-positioners excel in stability [13]. Hybrid nano-positioners [14,15] combine principles for precision and adaptability, revolutionizing nanoscale control [16]. Lorentz actuators excel in high-precision positioning due to their low mechanical stiffness, linear current-force relation, and favorable dynamics. This stiffness minimizes external motion transfer, caused by vibrations or actuator reaction forces, reducing support structure resonances. However, Lorentz actuators have limitations, such as a modest force constant limiting acceleration and stroke [17]. The Hybrid Reluctance Actuator (HRA) combines the principles of reluctance and permanent magnetism, offering improved force-to-weight ratios and enhanced linearity. As a result, HRAs have found value in a range of applications, including metrology, optical scanning, system stabilization, material processing, and semiconductor manufacturing. Their reliability is especially advantageous for system stabilization, while their efficient actuation contributes to material processing efficiency. In the semiconductor manufacturing industry, HRAs play a pivotal role in achieving precise and consistent results [18–20]. These innovations have significantly advanced the field of nanoscale control.

Xinyi Su et al. achieved a satisfactory accuracy in calculating the electromagnetic forces for HRAs by comparing the electromagnetic force in analytical models with finite element analysis (FEA) methods [21]. Kluk et al. focused on modeling and disregarded the influence of coil current in the permanent magnet branch [22]. Ito et al. considered the effects of field fringing and flux leakage, using a coefficient in the magnetic motive force of permanent magnet calculated through the FEM. These nonlinear effects were only taken into account in the permanent magnet and were neglected in air gaps and coils [18]. Weipan Zhang et al. achieved good accuracy in their modeling approach by designing HRAs while considering leakage in coils and permanent magnets and comparing it to the FEM method [21]. Laboreo et al. addressed various factors like input saturation, Eddy currents, flux fringing, and magnetic hysteresis for a single-coil HRA, comparing it with the FEM approach [23]. In another article, an HRA with two degrees of freedom was simulated using a multi physics finite element model, and its frequency response was validated and compared to two other systems' frequency responses [24].

In recent research endeavors, several innovative approaches have been explored to enhance the precision and performance of reluctance actuators. These methods aim to address inherent nonlinearities [25], improve linearity, and reduce susceptibility to disturbances, ultimately striving for superior positioning capabilities. In this introduction, the key findings and challenges encountered in these pioneering studies will be briefly overviewed. One notable advancement in this field is the application of feedback linearization techniques by Ines Burgstaller [26]. Their approach promises smooth and high-precision positioning, marking a significant step forward in the realm of the nano-positioner systems. However, it is important to note that the successful implementation of this method demands meticulous modeling precision and operates optimally within specific operational parameters. Challenges may arise, particularly in scenarios involving slow motion, making it imperative for engineers to consider precise engineering considerations during implementation. Another promising avenue explored by Ito et al. involves the control strategy for sample-tracking vibration isolators using HRAs [19]. Their strategy incorporates a PID controller with phase lead and notch filters, resulting in improved precision, enhanced vibration rejection, and faster response times. Nevertheless, this approach faces challenges related to parameter sensitivity and limitations when dealing with frequencies beyond the designed notch filters, underscoring the need for careful parameter tuning and consideration of system constraints. Ernst has contributed to the field by developing a control method for HRAs aimed at achieving precise position control by shaping the frequency response to meet performance requirements. This approach offers advantages such as decoupled control and flexibility with PID controllers [27]. However, it presents challenges related to Eddy currents, controller complexity, and sensitivity to sampling frequency, underscoring the importance of accounting for these factors in practical applications. In a quest for energy efficiency, Ito et al. have investigated a gravity compensation method for HRAs utilizing zero-current control [4]. This approach reduces power consumption during gravity compensation while maintaining system stability and precision. However, it introduces complexities and limitations, such as hysteresis and critical velocity constraints, which require careful management in real-world applications. Kluk has designed an orientation-independent system for effective operation, addressing challenges posed by hysteresis and critical velocity limits [22]. While his system is suitable for low-velocity movements, it may not be well-suited for high-speed applications. Additionally, sensitivity to external vibrations in the current control loop's bandwidth may necessitate additional measures for stability and accuracy in the presence of disturbances. In the pursuit of nano-positioner stability, Ito et al. have focused on feedback control, employing lead compensators, notch filters, and PI controllers [18]. They have introduced modeling-free Iterative Integral Control (IIC) for nonlinear compensation, offering adaptability but potentially longer convergence times. Precision sensors are of utmost importance in this context, as inaccuracies can disrupt nano-positioner, emphasizing the need for sensor precision to ensure system reliability and performance.

In the realm of modeling, various non-structural uncertainties such as Eddy currents, hysteresis losses, input saturation [28], field fringing, Electromagnetic Interference (EMI), and flux leakage have been carefully taken into account. Different control methods, including linear feedback control [29], PID control, and current control, have been applied [4,19,22,23,26,30]. To reduce the complexity in the governing equations of the control system, specific assumptions have been made, resulting in the linearization and simplification of control system equations. Additionally, software tools like Maxwell, ANSYS have been employed to gauge the extent of nonlinear effects caused by these factors [18,22].

The subsequent sections of this article are structured as follows: Section 2 encompasses the comprehensive modeling of the system and the extraction of open-loop equations. It introduces a second-order linear oscillatory actuator, bridging the control input and voltage, formulates the system state-space equations, and employs the Adams-Bashforth and Adams-Moulton methods for discretization. Furthermore, it presents a hybrid two-mode control algorithm based on reaching law principles. The section also addresses the integration of actuation system constraints into the desired trajectory filtering

mechanism, the switching control mode mechanism, and the utilization of an adaptive lookup table for control input calculation. In Section 3, the simulation procedure is elucidated, outlining the systematic process with the defined parameters within the relevant setup. Subsequently, a comprehensive analysis of the simulation results is provided, accompanied by detailed explanations and pertinent examinations. These outcomes effectively illustrate the performance of the control system. At the end, Section 4 serves as a culmination of this research endeavor, summarizing the findings and evaluating the performance of the proposed control system in the conclusion.

2. Control System Modelling

In this section, we initially elucidate the process of designing and implementing the control system. Subsequently, the scrutinized system is comprehensively delineated, and its equations are extracted in detail. Following the derivation of the open-loop system equations, a control algorithm has been designed, and its functional structure can be observed in Fig. 1.

Based on the closed-loop system considering the mathematical model of the vibratory mass coupled with an electromagnetic actuator, an appropriate control algorithm for trajectory tracking can be designed as depicted in Fig. 1. In this article, at first the continuous-time system equations are discretized to obtain a prediction of the system dynamics. Using the discretized equations and stable reaching laws for both position and velocity control modes, the electromagnetic force is computed. These reaching laws are designed to establish a relationship between the tracking error in the current and future time steps. Employing both position and velocity control modes ensures that when one of the reaching laws is not satisfied due to actuation system constraints, the other mode remains stable, ensuring overall system stability at all times. Considering the operational limitations of the actuator, such as saturation limits and natural frequency constraints, it's possible that in some situations, the reaching law may lose its stability, resulting in degraded tracking performance. Therefore, it's crucial to take into account these actuation system constraints in the control system design. This aim is achieved by filtering the desired trajectory using a filtering mechanism. By filtering the position and velocity references, confidence can be maintained that the system's closed-loop stability is preserved even in the presence of actuator limitations. To calculate the electromagnetic force for each of the position and velocity control modes, the final electromagnetic force must be determined in a switching manner between these control modes. This is accomplished by comparing the predictive tracking error between the two control modes, and the optimal mode is selected. The use of the weighting factor W_{pv}, which represents the significance of velocity tracking error in the cost function of the comparator, allows for the adjustment of the control system's behavior. Once the required electromagnetic force for system control is determined, the corresponding control input must be calculated. This is achieved using an adaptive lookup table that is designed to map control inputs to various electromagnetic force levels within the saturation limits. This table requires real-time updates to adapt to varying system conditions [31],[32].

2.1. Open Loop Equations of HRA

In this section, the open-loop system equations are first derived and subsequently utilized for the design of the control system. The desired system in the Fig. 2-a consists of a ferrous core (iron yoke), a permanent magnet, a coil on the left side, and a movable mass with flexible supports at a specified distance from the ferrous core. The permanent magnet, by generating a constant and stable magnetic flux, allows it to overcome the equivalent stiffness of the flexible supports. The coil on the left side is also powered by a voltage source.

To obtain the governing equations for this system, one should start by constructing the equivalent electromagnetic circuit [22]. Then, by applying Kirchhoff's laws, the fluxes through each of the three paths within the ferrous core can be determined. Next, utilizing the Maxwell stress tensor, the resulting force generated by the variable flux can be computed. Lastly, by applying Newton's second law, the differential equations that govern the HRA system dynamics can be derived.

2.1.1. Equivalent Circuit of HRA

According to the diagram in Fig. 2-b, the equivalent circuit for the electromagnetic part of the system is drawn under the following set of assumptions:

- The iron core is considered ideal.
- Field fringing effects are neglected.

- Magnetic leakage in the permanent magnet and coil is disregarded.
- A constant permeability of the core material is assumed.

As shown in the Fig. 2-b, there are four resistances in order from left to right, R_L represents the air resistance between the movable mass and the iron core on the left side, R_P represents the resistance of the permanent magnet, R_A represents the air resistance between the movable mass and the permanent magnet, and R_R represents the air resistance between the movable mass and the iron core on the right side. The relationships for these resistances are as shown in Eq. (1).

$$R_P = \frac{l_p}{\mu_0 A}, R_A = \frac{l_A}{\mu_0 A}, R_L = \frac{x_g - x}{\mu_0 A}, R_R = \frac{x_g + x}{\mu_0 A}, R_M = \frac{l_p + l_A}{\mu_0 A} \quad (1)$$

Where χ x is the position of the movable mass, and x_g is the distance of the movable mass from either side of the iron core at $x = 0$. l_P and l_A represent the length of the permanent magnet and the constant air gap distance between the permanent magnet and the movable mass respectively. The μ_0 is the permeability of the air, and A is the cross-sectional area through which magnetic flux passes perpendicular to it. The coil and the permanent magnet are sources of magnetic flux. The magnetic driving force produced by the coil and the permanent magnet is described in Eqs. (2), (3).

$$\Psi_C = NI \quad (2)$$

$$\Psi_P = M_0 l_P \quad (3)$$

Where N is the number of turns of the coil, M_0 is the magnetic field strength per unit length for the permanent magnet, and I is the current passing through the coil. By applying Kirchhoff's Voltage Law (KVL) and Kirchhoff's Current Law (KCL), the magnetic fluxes on the left and right sides of the circuit are determined, as described in Eqs. (4), (5). Given that a voltage source is used to drive the current in the coils, V is the applied voltage, and R is the resistance of the coil's wire. The voltage across the coil is equal to the self-induced voltage in the coil plus the voltage drop across the coil's resistance, as mentioned in Eq. (6).

$$\Phi_L = \frac{\left[\Psi_C \left(R_R + R_M\right) - \Psi_P R_R\right]}{\left[R_M \left(R_L + R_R\right) + R_L R_R\right]} \quad (4)$$

$$\Phi_R = \frac{-\Psi_C R_M - \Psi_P R_L}{\left[R_M \left(R_L + R_R\right) + R_L R_R\right]} \quad (5)$$

$$v = IR + N \frac{d\Phi_L}{dt} \quad (6)$$

Eq. (7) represents the governing equation between the applied voltage and the generated current in the coil. In this equation, the coefficient $a(x)$ is a function of the position of mass M and can be calculated using Eq. (8). Additionally, the other components of the equation, which are functions of current, position, and velocity of mass M, are represented by the term $b(I, x, \dot{x})$, and they can be computed using Eq. (9).

$$a(x)\dot{I} = b(I, x, \dot{x}) + v \quad (7)$$

$$a(x) = \mu_0 A N^2 \frac{(x_g + x) + (l_p + l_A)}{x_g^2 - x^2 + (l_p + l_A)(2x_g)} \quad (8)$$

$$b(I,x,\dot{x}) = \Theta_b(x,\dot{x})I + \Upsilon_b(x,\dot{x}) \tag{9}$$

In which, the terms $\Theta_b(x,\dot{x})$ and $\Upsilon_b(x,\dot{x})$ can be computed using Eqs. (10), (11), respectively.

$$\Theta_b(x,\dot{x}) = -\frac{\mu_0 AN^2\dot{x}}{x_g^2 - x^2 + (l_p + l_A)(2x_g)} - \frac{2\mu_0 AN^2 x\left[(x_g + x) + (l_p + l_A)\right]\dot{x}}{\left[x_g^2 - x^2 + (l_p + l_A)(2x_g)\right]^2} - R \tag{10}$$

$$\Upsilon_b(x,\dot{x}) = +\frac{\mu_0 ANM_0 l_P\dot{x}}{x_g^2 - x^2 + (l_p + l_A)(2x_g)} + \frac{2\mu_0 ANM_0 l_P x(x_g + x)\dot{x}}{\left[x_g^2 - x^2 + (l_p + l_A)(2x_g)\right]^2} \tag{11}$$

Furthermore, the fluxes generated in the left and right halves of the iron yoke can be computed as functions of the current and the position of mass M, respectively, using Eqs. (12), (13).

$$\Phi_L = \Theta_\Phi^L(x)I + \Upsilon_\Phi^L(x) \tag{12}$$

$$\Phi_R = \Theta_\Phi^R(x)I + \Upsilon_\Phi^R(x) \tag{13}$$

where the terms $\Theta_\Phi^L(x)$, $\Upsilon_\Phi^L(x)$, $\Theta_\Phi^R(x)$, and $\Upsilon_\Phi^R(x)$ can be obtained using Eqs. (14)-(17).

$$\Theta_\Phi^L(x) = \frac{\mu_0 AN\left[(x_g + x) + (l_p + l_A)\right]}{x_g^2 - x^2 + (l_p + l_A)(2x_g)} \tag{14}$$

$$\Upsilon_\Phi^L(x) = -\frac{\mu_0 AM_0 l_p(x_g + x)}{x_g^2 - x^2 + (l_p + l_A)(2x_g)} \tag{15}$$

$$\Theta_\Phi^R(x) = -\frac{\mu_0 AN(l_p + l_A)}{x_g^2 - x^2 + (l_p + l_A)(2x_g)} \tag{16}$$

$$\Upsilon_\Phi^R(x) = -\frac{\mu_0 AM_0 l_p(x_g - x)}{x_g^2 - x^2 + (l_p + l_A)(2x_g)} \tag{17}$$

As evident from the equations, the magnitudes of magnetic fluxes, coil current intensity, and the electromagnetic force are dependent on the position and velocity of the vibrating mass. To investigate the effects of the position and velocity of the vibrating mass on the mentioned variables, Fig. 3 has been presented. In this figure, the fluxes on the left and right sides, the coil current, and the electromagnetic force are plotted for different values of the position and velocity of the vibrating mass.

As observed in Fig. 3, when the vibrating mass moves towards positive values, the magnetic flux in the left branch decreases, the magnetic flux in the right branch increases, and the electromagnetic force decreases. Meanwhile, the coil current intensity remains nearly constant. Additionally, with an increase in the velocity of the vibrating mass, the magnetic flux in the left branch increases, the magnetic flux in the right branch decreases, and both the coil current and electromagnetic force increase. Therefore, the position and velocity of the vibrating mass play a significant role in the open-loop equations of the control system, and they should be carefully considered in the control algorithm.

2.1.2. Dynamics Equations of Moving Part of the HRA

Taking into account the fluxes generated in the left and right sides of the iron core, as shown in Fig. 2, the equation of motion for mass M will be as Eq. **Error! Reference source not found.**, where k_0 is the linear spring coefficient, C_0 is the linear d amping coefficient, k_1 is the nonlinear spring coefficient, and C_1 is the nonlinear damping coefficient.

$$M\ddot{x} = \frac{1}{2\mu_0 A}\left[\Phi_L^2 sgn(\Phi_L) - \Phi_R^2 sgn(\Phi_R)\right] - k_0 x - k_1 x^3 - c_0\dot{x} - c_1\dot{x}^2 sgn(\dot{x}) \quad (18)$$

Eq. (18) can be rewritten as Eq. (19), in which the actuating force, denoted as u, can be calculated from Eq. (20).

$$M\ddot{x} = u - k_0 x - k_1 x^3 - c_0\dot{x} - c_1\dot{x}^2 sgn(\dot{x}) \quad (19)$$

$$u \triangleq \frac{1}{(2\mu_0 AM)}[\Phi_L^2 sgn(\Phi_L) - \Phi_R^2 sgn(\Phi_R)] \quad (20)$$

2.1.3. Second-Order Linear Oscillatory Actuation System

The control system actuator is considered as a second-order dynamic system, and by applying the control input v_c, one can control the actuator's output, namely, the voltage v. Eq. (21) represents the transfer function governing the relationship between the control input v_c and the voltage v. This transfer function can be rewritten in the time domain as Eq. (22).

$$\frac{v}{v_c} = \frac{(\omega_0^2)}{(s^2 + 2\xi\omega_0 s + \omega_0^2)} \quad (21)$$

$$\ddot{v} + 2\xi\omega_0\dot{v} + \omega_0^2 v = \omega_0^2 v_c \quad (22)$$

In which, ξ is the damping coefficient, and ω_0 is the natural frequency of the actuator, which will determine the second-order dynamic behavior of the actuator. By discretizing Eq. (22) using Adams-Moulton discretizing method [33], it is possible to calculate the voltage at time index $k-1$, representing the current time step, as a function of the control input in Eq. (23). The discretization of Eq. (22) is performed using the Adams-Moulton discretizing method. Following the extraction of state equations for the second-order equation, each of the state equations can be discretized, and the relationship between v and v_c can be extracted discretely.

$$v(k-1) = pv_c(k-1) + q(k-1) \quad (23)$$

Wherein, the control input coefficient p can be calculated using Eq. (24), and the term $q(k-1)$, which includes past terms of the actuator dynamics, can be calculated using Eq. (25).

$$p \triangleq \frac{T^2\omega_0^2}{T^2\omega_0^2 + 4\xi T\omega_0 + 4} \quad (24)$$

$$q(k-1) \triangleq \frac{-(2T^2\omega_0^2 - 8)}{(T^2\omega_0^2 + 4\zeta T\omega_0 + 4)}v(k-2) - \frac{(T^2\omega_0^2 - 4\zeta T\omega_0 + 4)}{(T^2\omega_0^2 + 4\zeta T\omega_0 + 4)}v(k-3) \quad (25)$$
$$+ \frac{T^2\omega_0^2}{(T^2\omega_0^2 + 4\zeta T\omega_0 + 4)}v_c(k-3) + \frac{2T^2\omega_0^2}{(T^2\omega_0^2 + 4\zeta T\omega_0 + 4)}v_c(k-2)$$

Furthermore, by discretizing Eq. (7) using the Adams-Moulton method [33], the coil current can be calculated as a function of voltage within a time step. Subsequently, substituting Eq. (23) into the discretized version of Eq. (7) will yield Eq. (26), which represents the relationship between $I(k-1)$ and the control input (command), namely $v_c(k-1)$.

$$I(k-1) = \Omega(k-1)v_c(k-1) + \Gamma(k-1) \quad (26)$$

Wherein, the coefficient $\Omega(k-1)$ can be calculated using Eq. (27), and the terms containing the past dynamics of the coil, as per Eq. (28), will be stored in $\Gamma(k-1)$.

$$\Omega(k-1) = \left[1 - \frac{T}{2a(k-1)}\Theta_b(k-1)\right]^{-1} \frac{Tp}{2a(k-1)} \tag{27}$$

$$\Gamma(k-1) = [1 - \frac{T}{2a(k-1)}\Theta_b(k-1)]^{-1} \left\{ \begin{array}{l} I(k-2) + \frac{T}{2a(k-1)}[\Upsilon_b(k-1) + q(k-1)] + \\ \frac{T}{2a(k-2)}[\Theta_b(k-2)I(k-2) + \Upsilon_b(k-2) + v(k-2)] \end{array} \right\} \tag{28}$$

2.2. Two-Mode (Position-Velocity Hybrid) Control Algorithm

By considering the open-loop dynamic equation of the system in the form of Eq. (29), it is possible to calculate the system's acceleration at each moment by applying the electromagnetic force u. In this equation, the term $g(x, \dot{x})$ is a function of the position and velocity of mass M and can be calculated using Eq. (30).

$$\ddot{x} = u + g(x, \dot{x}) \tag{29}$$

$$g(x, \dot{x}) = \frac{-k_0}{M}x - \frac{k_1}{M}x^3 - \frac{c_0}{M}\dot{x} - \frac{c_0}{M}\dot{x}^2 sgn(\dot{x}) \tag{30}$$

Continuing with the dynamic equation of the system represented by Eq. (29), it is possible to design a control algorithm in two modes: position control and velocity control. To achieve this, considering the tracking error in position and velocity at each time step and defining stable reaching laws for each control mode, the electromagnetic force required to satisfy the reaching law will be calculated. On the other hand, the control input is subjected to saturation limits, and the natural frequency of the actuator's dynamics imposes constraints on the electromagnetic force. The upper and lower bounds of these constraints need to be determined at each time step. Therefore, it is necessary to use a filtering algorithm for the desired trajectory while taking into account the system's actuator constraints. This ensures the stability of the closed-loop control system. The calculation of the electromagnetic force is performed in both position and velocity control modes, guaranteeing that if stability conditions are not satisfied for one control mode, the other control mode will continue to follow the desired trajectory in a stable manner. In this way, the tracking error in at least one of the control modes is minimized, ensuring the stability of the closed-loop system [32–34]. After calculating the electromagnetic force required for system control in each control mode, an optimal control mode can be determined by performing a search along the system's dynamics. Once the necessary electromagnetic force for controlling the system is determined, an adaptive lookup table can be used to establish the relationship between the electromagnetic force and the control input at each time step. This enables the calculation of the corresponding control input for the given electromagnetic force, which can then be applied to the actuator.

2.2.1. State Space Variables and Discretization

To write the dynamic equations of the system in state space, the state variables can be defined as follows: $x_1 = x$ for position and $x_2 = \dot{x}$ for velocity. Consequently, the state equations of the system can be written as Eqs. (31), (32).

$$\dot{x}_1 = x_2 \tag{31}$$

$$\dot{x}_2 = g(x, \dot{x}) + u \tag{32}$$

To consider the dynamic behavior of the system, it is necessary to discretize the governing equations, and this is done using the Adams-Bashforth and Adams-Moulton methods [33]. By using the Adams-Moulton method to discretize Eq. (31), the position of mass M can be calculated in Eq. (33), where the position at time k is calculated based on the velocity at time k

. Consequently, it is necessary to calculate the velocity at time k, which can be done by discretizing Eq. (32) using the Adams-Bashforth method to calculate the velocity from Eq. (34).

$$x_1(k) = x_1(k-1) + \frac{T}{2}x_2(k) + \frac{T}{2}x_2(k-1) \tag{33}$$

$$x_2(k) = x_2(k-1) + \frac{3T}{2}\left[g(k-1) + u(k-1)\right] - \frac{T}{2}\left[g(k-2) + u(k-2)\right] \tag{34}$$

As observed in Eqs. (33), (34), the position and velocity of the system at time k depend on the electromagnetic force $u(k-1)$. By substituting Eq. (34) into Eq. (33), the electromagnetic force $u(k-1)$ appears in the equation for calculating the position. Therefore, by applying the electromagnetic force, the position of the system can be calculated using Eq. (35), and the velocity of the system can be calculated using Eq. (36).

$$x_1(k) = \xi_p(k-1) + \mu_p u(k-1) \tag{35}$$

$$x_2(k) = \xi_v(k-1) + \mu_v u(k-1) \tag{36}$$

Where $\xi_p(k-1)$ and $\xi_v(k-1)$ include the past terms of the system's dynamics and are calculated using Eqs. (37), (38). Additionally, the coefficient of $u(k-1)$ in the equations for position and velocity is represented by symbols μ_p and μ_v, respectively, which can be calculated using Eqs. (39), (40).

$$\xi_p(k-1) = x_1(k-1) + \frac{T}{2}\left[x_2(k-1) + \frac{3T}{2}g(k-1) - \frac{T}{2}[g(k-2) + u(k-2)]\right] + \frac{T}{2}x_2(k-1) \tag{37}$$

$$\xi_v(k-1) = x_2(k-1) + \frac{3T}{2}g(k-1) - \frac{T}{2}[g(k-2) + u(k-2)] \tag{38}$$

$$\mu_p = \frac{3T^2}{4} \tag{39}$$

$$\mu_v = \frac{3T}{2} \tag{40}$$

In this way, by discretizing the equations, the position and velocity of the system at time step k can be obtained as functions of $u(k-1)$, which will be used in the controller design.

2.2.2. Power Reaching Law Based Controller Design

In stable reaching law of Eq. (41), $\eta_{CM}(k-1)$ represents the stability coefficient for the position or velocity control mode and must have values smaller than 1 to maintain the stability of the reaching law. Since equations for both position and velocity modes will be written below, a common symbol CM is used, where $CM \to p$ refers to the position mode, and $CM \to v$ refers to the velocity mode.

$$s_{CM}(k) = \eta_{CM}(k-1)\, s_{CM}(k-1); \left|\eta_{CM}(k-1)\right| < 1 \tag{41}$$

In Eq. (41), the current-time error in position or velocity tracking, represented by $s_p(k-1)$ and $s_v(k-1)$ respectively, replaces $s_{CM}(k-1)$. These errors are calculated using Eqs. (42), (43).

$$s_p(k-1) = \tilde{x}(k-1) = x_1(k-1) - x_d(k-1) \tag{42}$$

$$s_v(k-1) = \dot{\tilde{x}}(k-1) = x_2(k-1) - \dot{x}_d(k-1) \tag{43}$$

In Eqs. (42) and (43) $x_d(k-1)$ and $\dot{x}_d(k-1)$ represent the current-time position and velocity of the desired trajectory, respectively, and they are utilized for error calculation. As demonstrated in Eqs. (35), (36), it is feasible to express the right-hand side of the equations as $\xi_{CM}(k-1) + \mu_{CM} u(k-1)$ and by its substitution into Eq. (41), Eq. (44) is derived.

$$\xi_{CM}(k-1) + \mu_{CM} u(k-1) - x_{dCM}(k) = \eta_{CM}(k-1) s_{CM}(k-1) \tag{44}$$

In this context, $\xi_{CM}(k-1)$ is computed for the position mode using Eq. (37) and for the velocity mode using Eq. (38). Additionally, μ_{CM} can be calculated for the position mode using Eq. (39) and for the velocity mode using Eq. (40). $x_{dCM}(k)$ is also assumed to be equal to $x_d(k)$ for the position mode and equal to $\dot{x}_d(k)$ for the velocity mode. Consequently, it becomes feasible to derive the electromagnetic force associated with each control mode using Eq. (45).

$$u_{CM}(k-1) = \frac{1}{\mu_{CM}} \left[\eta_{CM}(k-1) s_{CM}(k-1) - \xi_{CM}(k-1) + x_{dCM}(k) \right] \tag{45}$$

2.2.3. Control Input Saturation Constraint

As observed, the electromagnetic force for tracking the desired trajectory in both position and velocity control modes of the system was calculated according to Eq. (45). On the other hand, the electromagnetic force $u(k-1)$ is a function of $\Phi_L(k-1)$ and $\Phi_R(k-1)$ according to Eq. (20). Through discretization of this relationship, Eq. (46) is derived.

$$u(k-1) = \frac{1}{2\mu_0 AM} \left\{ [\Phi_L(k-1)]^2 \operatorname{sgn}[\Phi_L(k-1)] - [\Phi_R(k-1)]^2 \operatorname{sgn}[\Phi_R(k-1)] \right\} \tag{46}$$

By substituting Eq. (26) into Eqs. (12), (13), $\Phi_L(k-1)$ and $\Phi_R(k-1)$ can be discretized as functions of the control input $v_c(k-1)$ and the results are represented as Eqs. (47), (48).

$$\Phi_L(k-1) = \Theta_\Phi^L(k-1)[\Omega(k-1) v_c(k-1) + \Gamma(k-1)] + \Upsilon_\Phi^L(k-1) \tag{47}$$

$$\Phi_R(k-1) = \Theta_\Phi^R(k-1)[\Omega(k-1) v_c(k-1) + (k-1)] + \Upsilon_\Phi^R(k-1) \tag{48}$$

According to Eq. (49), it is evident that $u(k-1)$ will be a function of $v_c(k-1)$ and past dynamics. Therefore, the presence of constraints on the system actuator will impose constraints on the electromagnetic force, which need to be considered in the controller design.

$$u(k-1) = \frac{1}{2\mu_0 AM} \begin{Bmatrix} [\Theta_\Phi^L(k-1)[\Omega(k-1) v_c(k-1) + \Gamma(k-1)] + \Upsilon_\Phi^L(k-1)]^2 \\ sgn[\Theta_\Phi^L(k-1)[\Omega(k-1) v_c(k-1) + \Gamma(k-1)] + \Upsilon_\Phi^L(k-1)] \\ -[\Theta_\Phi^R(k-1)[\Omega(k-1) v_c(k-1) + \Gamma(k-1)] + \Upsilon_\Phi^R(k-1)]^2 \\ sgn[\Theta_\Phi^R(k-1)[\Omega(k-1) v_c(k-1) + \Gamma(k-1)] + \Upsilon_\Phi^R(k-1)] \end{Bmatrix} \tag{49}$$

Subsequently, by imposing the saturation limit on the system actuator, defined as $|v_c(k-1)| \le v_0$, the permissible range for calculating $u(k-1)$ will be determined. To achieve this, the derivative of $u(k-1)$ with respect to $v_c(k-1)$ can be obtained using the chain rule, as shown in Eq. (50).

$$\frac{\partial u(k-1)}{\partial v_c(k-1)} = \frac{\partial u(k-1)}{\partial \Phi_L(k-1)} \frac{\partial \Phi_L(k-1)}{\partial I(k-1)} \frac{\partial I(k-1)}{\partial v_c(k-1)} + \frac{\partial u(k-1)}{\partial \Phi_R(k-1)} \frac{\partial \Phi_R(k-1)}{\partial I(k-1)} \frac{\partial I(k-1)}{\partial v_c(k-1)} \quad (50)$$

By computing the partial derivatives in Eq. (50), Eq. (51) is obtained.

$$\frac{\partial u(k-1)}{\partial v_c(k-1)} = \Omega(k-1) \frac{\Phi_L(k-1) sgn[\Phi_L(k-1)] \Theta_\Phi^L(k-1) - \Phi_R(k-1) sgn[\Phi_R(k-1)] \Theta_\Phi^R(k-1)}{\mu_0 AM} \quad (51)$$

Therefore, by setting $\frac{\partial u(k-1)}{\partial v_c(k-1)}$ to zero, extremum points can be calculated. By comparing these points with the boundary points of $u(k-1)$ with respect to $v_c(k-1)$, the maximum and minimum values of $u(k-1)$ can be determined. These maximum and minimum values, denoted as $u_{\max}(k-1)$ and $u_{\min}(k-1)$ can then be presented in Eq. (52).

$$u_{\min}(k-1) \le u_{CM}(k-1) \le u_{\max}(k-1) \quad (52)$$

2.2.4. Actuator Saturation Effects on Desired Trajectory

Upon determining the upper and lower bounds of $u_{CM}(k-1)$, these constraints can be incorporated into the control algorithm. By substituting $u_{CM}(k-1)$ from Eq. (45) into Eq. (52), the inequality for $x_{dCM}(k)$ can be expressed as Eq. (53).

$$Q_{lCM}(k-1) \le x_{dCM}(k) \le Q_{uCM}(k-1) \quad (53)$$

Where $Q_{lCM}(k-1)$ and $Q_{uCM}(k-1)$ represent the lower and upper bounds of $x_{dCM}(k)$ and they are computed using Eqs. (54), (55), respectively.

$$Q_{lCM}(k-1) \triangleq \mu_{CM} u_{\min}(k-1) - \eta_{CM}(k-1) s_{CM}(k-1) + \xi_{CM}(k-1) \quad (54)$$

$$Q_{uCM}(k-1) \triangleq \mu_{CM} u_{\max}(k-1) - \eta_{CM}(k-1) s_{CM}(k-1) + \xi_{CM}(k-1) \quad (55)$$

As evident in Eqs. (54), (55), the upper and lower bounds of $x_{dCM}(k)$ are functions of $\eta_{CM}(k-1)$, which, according to the defined reaching law, can assume values smaller than one. However, it is possible that at some points, $x_{dCM}(k)$ may fall outside the interval defined in Eq. (53). Consequently, a suitable control input may not be found within the operating range of the actuator, jeopardizing the stability of the closed-loop system. To address this concern, the control system will track the filtered value of $x_{dCM}(k)$, denoted as $\hat{x}_{dCM}(k)$, which can be computed using a trajectory filtering mechanism.

2.2.5. Desired Trajectory Filtering Mechanism

In this section, the operation of the trajectory filtering mechanism is explained. This mechanism works as follows: for each $\eta_{CM}^i(k-1) \in (-1, +1)$, first, the upper and lower bounds of $x_{dCM}^i(k)$ are calculated using Eqs. (56), (57).

$$Q_{lCM}^i(k-1) \triangleq \mu_{CM} u_{\min}(k-1) - \eta_{CM}^i(k-1) s_{CM}(k-1) + \xi_{CM}(k-1) \quad (56)$$

$$Q_{uCM}^i(k-1) \triangleq \mu_{CM} u_{\max}(k-1) - \eta_{CM}^i(k-1) s_{CM}(k-1) + \xi_{CM}(k-1) \quad (57)$$

Then, $\hat{x}_{dCM}^i(k)$ can be calculated as the closest value to $x_{dCM}(k)$ that falls within the allowable range. In this way, for each $\eta_{CM}^i(k-1)$, one $\hat{x}_{dCM}^i(k)$ will be obtained. Using the cost function $J_{CM}(k-1)$ introduced in Eq. (58), a comparison

can be made between the obtained $\hat{x}^i_{dCM}(k)$'s, and the closest value to $x_{dCM}(k)$ can be found by minimizing the cost function $J_{CM}(k-1)$. Thus, the filtered value of the desired trajectory for the next time step, along with its corresponding stability coefficient, is calculated, denoted as $\hat{x}^*_{dCM}(k)$ and $\eta^*_{CM}(k-1)$, respectively.

$$J_{CM}(k-1) = [\hat{x}^i_{dCM}(k) - x_{dCM}(k)]^2 \Rightarrow \hat{x}^*_{dCM}(k), \eta^*_{CM}(k-1) \tag{58}$$

With $\hat{x}^*_{dCM}(k)$ and $\eta^*_{CM}(k-1)$ determined, the electromagnetic force $u^*_{CM}(k-1)$, which satisfies the actuator constraints, can be calculated for each of the position and velocity control modes using Eq. (59).

$$u^*_{CM}(k-1) = \frac{1}{\mu_{CM}}[\eta^*_{CM}(k-1)s_{CM}(k-1) - \xi_{CM}(k-1) + \hat{x}^*_{dCM}(k)] \tag{59}$$

2.2.6. Control Mode Switching Mechanism

As seen in the previous sections, electromagnetic forces for each of the position and velocity control modes, denoted as $u^*_p(k-1)$ and $u^*_v(k-1)$ respectively, were obtained using Eq. (59). Among these two electromagnetic forces, each of which reduces the tracking error of its corresponding mode, the optimal mode can be selected by comparing based on the prediction error. To do this, the cost function $G(k-1)$ is defined as the weighted sum of prediction errors for position and velocity tracking, as per Eq. (60). This cost function is computed at each time step, twice for $u(k-1) = u^*_p(k-1)$ and $u(k-1) = u^*_v(k-1)$, and among these two, the desired solution is the one with the smaller cost function. In this way, the optimal control mode can be determined at each time step.

$$G(k-1) = [x_1(k) - x_d(k)]^2 + W_{pv}[x_2(k) - \dot{x}_d(k)]^2 \tag{60}$$

As shown in Eq. (60), the cost function $G(k-1)$ is formulated as the weighted sum of prediction errors for position and velocity tracking, where the coefficient W_{pv} determines the importance of selecting position or velocity control mode as the optimal control mode. When the value of W_{pv} is smaller, the controller places more emphasis on reducing position tracking error compared to velocity tracking error, and vice versa. Thus, by properly tuning the W_{pv} coefficient, the behavior of the control system, including the speed of reaching the desired trajectory and the magnitude of overshoot/undershoot, can be adjusted.

2.2.7. Adaptive Look-Up Table of Inverse Dynamics of Electromagnetic Force

To determine the appropriate $v_c(k-1)$ that can generate the required electromagnetic force $u(k-1)$ after selecting the optimal control mode and calculating $u(k-1)$, it is necessary to create a lookup table between $v_c(k-1)$ values and different $u(k-1)$ values. This lookup table can be generated after determining $u_{\max}(k-1)$ and $u_{\min}(k-1)$ as follows: For a range of $v_c(k-1)$ values within the actuator's saturation limits and considering the calculated extreme values, various $u(k-1)$ values are computed. By creating this lookup table, it becomes possible to determine the nearest $v_c(k-1)$ that can produce the desired electromagnetic force after calculating $u(k-1)$ using the control algorithm. Naturally, a higher resolution lookup table will provide more precise control, allowing $v_c(k-1)$ to apply $u(k-1)$ more accurately and improving the overall system control performance.

2.3. Control Mode Switching Stability Proof

As observed in Section 2.2, if the electromagnetic force is applied to the system in the form of $u^*_{CM}(k-1)$, the filtered desired trajectory $\hat{x}_{dCM}(k)$ will be stably tracked. This is ensured in each of the position and velocity control modes by the reaching law Eq. (41), where $|\eta^*_{CM}(k-1)|<1$ holds true. However, it should be noted that with the use of the presented control algorithm for each of the control modes, instead of applying $u^*_{CM}(k-1)$ to the system, $u(k-1)$ is employed, which is dynamically switching between electromagnetic forces of the two control modes. Therefore, it can no longer be stated that the aforementioned reaching law remains valid, and an alternative reaching law is established in the system, as can be observed in Eq. (61), where $\eta'_{CM}(k-1) \neq \eta^*_{CM}(k-1)$ and $u(k-1) \neq u^*_{CM}(k-1)$.

$$\xi_{CM}(k-1)+\mu_{CM}u(k-1)-\hat{x}_{dCM}(k)=\eta'_{CM}(k-1)s_{CM}(k-1) \tag{61}$$

In other words, assuming $\alpha(k-1)=0$ or 1, $u(k-1)$ can be expressed as a linear combination of $u^*_{CM}(k-1)$ for both control modes, as shown in Eq. (62).

$$u(k-1)=\alpha(k-1)u^*_p(k-1)+[1-\alpha(k-1)]u^*_v(k-1) \tag{62}$$

By substituting Eq. (62) into Eq. (61), Eq. (63) will be obtained.

$$\begin{aligned}&\alpha(k-1)[\xi_p(k-1)+\mu_p u^*_p(k-1)-\hat{x}_d(k)]+[1-\alpha(k-1)][\xi_v(k-1)+\mu_v u^*_v(k-1)-\dot{\hat{x}}_d(k)] \\ &=\eta'_{CM}(k-1)s_{CM}(k-1)\end{aligned} \tag{63}$$

On the other hand, according to the reaching law of position control mode, $\xi_p(k-1)+\mu_p u^*_p(k-1)-\hat{x}_d(k)=\eta^*_p(k-1)s_{CM}(k-1)$, and by considering it in Eq. (63), Eq. (64) will be obtained.

$$\alpha(k-1)\eta^*_p(k-1)s_p(k-1)+[1-\alpha(k-1)][\xi_v(k-1)+\mu_v u^*_v(k-1)-\dot{\hat{x}}_d(k)]=\eta'_{CM}(k-1)s_{CM}(k-1) \tag{64}$$

Finally, assuming $s_{CM}(k-1)=s_p(k-1)\neq 0$ for position control mode, Eq. (64) can be represented as Eq. (65).

$$\eta'_{CM}(k-1)=\alpha(k-1)\eta^*_p(k-1)+[1-\alpha(k-1)]\frac{\xi_v(k-1)+\mu_v u^*_v(k-1)-\dot{\hat{x}}_d(k)}{s_p(k-1)} \tag{65}$$

In which, the coefficient $\alpha(k-1)$ can take on values of either zero or one. Setting $\alpha(k-1)=1$ results in the stability coefficient $\eta'_{CM}(k-1)=\eta^*_{CM}(k-1)$ for the position mode, while when $\alpha(k-1)=0$, $\eta'_{CM}(k-1)=\frac{\xi_v(k-1)+\mu_v u^*_v(k-1)-\dot{\hat{x}}_d(k)}{s_p(k-1)}$ is obtained, which, according to Eq. (44), is equal to $\eta^*_v(k-1)$ for the velocity mode. In both cases, it is observed that $|\eta'_{CM}(k-1)|<1$, indicating the stability of the reaching law introduced in Eq. (61).

Similarly, for the velocity control mode, Eqs. (64), (65) can be rewritten as Eqs. (66), (67).

$$\alpha(k-1)[\xi_p(k-1)+\mu_p u_p^*(k-1)-\hat{x}_d(k)]+[1-\alpha(k-1)]\eta_v^*(k-1)s_v(k-1)=\eta'_{CM}(k-1)s_{CM}(k-1) \quad (66)$$

$$\eta'_{CM}(k-1)=\alpha(k-1)\frac{[\xi_p(k-1)+\mu_p u_p^*(k-1)-\hat{x}_d(k)]}{s_v(k-1)}+[1-\alpha(k-1)]\eta_v^*(k-1) \quad (67)$$

In this case, if the coefficient $\alpha(k-1)$ is set to 0, then $\eta'_{CM}(k-1)$ will be equal to $\eta_v^*(k-1)$, and consequently, $|\eta'_{CM}(k-1)|<1$ will hold. When $\alpha(k-1)=1$ is chosen, as per Eq. (44), $\eta'_{CM}(k-1)$ equals $\eta_p^*(k-1)$, and again $|\eta'_{CM}(k-1)|<1$ is maintained. Thus, it is evident that the reaching law specified in Eq. (61) remains stable in this scenario as well [34].

Theorem 1. Consider a discrete single-degree-of-freedom system as described in Eq. (29). By appropriately applying $u(k-1)$ in the control system, the filtered desired trajectory presented will be effectively tracked by the controlled system. Furthermore, the filtered desired position and velocity can be stably achieved with the application of the electromagnetic force calculated in Eq. (45), even with constraints on the computation of electromagnetic force. In this case, by considering a linear combination of electromagnetic forces as presented in Eq. (62), where the coefficient $\alpha(k-1)$ can take values of either zero or one, the following proposition will hold true for time step $k-1$:

Proposition 1. If the coefficient $\alpha(k-1)$ is chosen such that Eq. (63) leads to $|\eta_{CM}(k-1)|<1$, then the filtered desired trajectory tracking will be stably achieved according to the reaching law presented in Eq. (61). Furthermore, the constraints imposed on the electromagnetic force due to the limitations of the voltage actuator system will never be violated.

3. Numerical Simulation Results and Discussions

In this section, to assess the performance of the proposed control algorithm in this paper, the control system's results are examined under various trajectory-tracking scenarios using numerical simulations in MATLAB software. Initial tuning of the control algorithm is carried out based on the derived equations in the previous sections, and numerical integration of the discretized equations allows for presenting the results in the form of plots. The simulation parameters used in these results are detailed in Table 1.

Table 1. Simulation parameters used in the paper along with descriptions

Simulation Parameter	Value	Explanation	Simulation Parameter	Value	Explanation
μ_0	$4\pi \times 10^{-7}$ [Wb/A. m]	Air Permeability	M	0.04 [Kg]	Mass
N_L	120	Coil Turns	c_0	4 [N. s/m]	Linear Damping Coeff.
l_P	19 [mm]	Length of Iron Core	k_0	1000000 [N/m]	Linear Spring Coeff.
l_A	1 [mm]	Distance of Mass from Iron Core	k_1	100 [N/m^3]	Nonlinear Spring Coeff.
x_g	1 [mm]	Gap Distance of Mass	c_1	1 [N. s^2/m^2]	Nonlinear Damping Coeff.
A	225 $\times$ 10^{-6} [m^2]	Magnetic Flux Area	T	0.00001 [sec]	Time Step Size
R	0.7 [Ω]	Coil Resistance	ω_0	2 [Rad/s]	Actuator Natural Frequency
M_0	10^6 [N/Wb]	Magnetic Field Strength	ξ	0.2	Actuator Damping Ratio

Given that the dynamical system operates on a nanometer scale, it is essential to carefully tune the simulation parameters. This includes setting the W_{pv} coefficient, which determines the behavior of the control system in tracking desired trajectories. The desired trajectories used for tracking operations have been configured in two scenarios: piecewise step and harmonic trajectories. The control relationships and parameters for each of them can be observed in Table 2.

Table 2. Desired trajectories considered for two tracking scenarios along with controller tuning parameters in the respective scenario

Scenario Parameter	piece wise step	harmonic
$\mathbf{x_d}$ [nm]	$\text{sign}(2\pi t)$	$\frac{1}{3}[-\cos(5t) - \cos(7t) + \cos(10t)]$
$\mathcal{V}_0$ [Volts]	0.7	0.05
$\mathbf{W_{pv}}$	0.3	0.95

Fig. 4 illustrates the results of position control of the system with the goal of trajectory tracking. In the tracking scenario of piecewise step, the control input is calculated by the control algorithm, taking into account the tracking error at the initial point of motion. The filtering mechanism calculates the filtered desired position. As shown in Fig. 4-a, the vibrating mass position tracks the filtered desired trajectory effectively. One characteristic of the piecewise step trajectory is the presence of sudden jumps in the trajectory, leading to a rapid increase in velocity. In these points, the control algorithm computes an infinite control input, while the control system actuator has saturation limits and cannot produce the required input to maintain system stability, resulting in control system instability. However, by filtering the desired trajectory based on the system actuator's constraints, the control algorithm calculates a reasonable control input within the actuator's saturation limits, preserving the stability of the closed-loop system. In the harmonic trajectory tracking scenario, as shown in Fig. 4-b, despite the continuous change in the desired trajectory and consequently the filtered desired trajectory, the vibrating mass's position effectively reduces the initial tracking error and eventually oscillates around the desired trajectory. The harmonic trajectory, which is a combination of different frequencies, highlights the sensitivity of the control algorithm to the frequency of the desired trajectory. Thus, the control system demonstrates minimal error and shows insensitivity to the frequency of the desired trajectory when performing harmonic trajectory tracking.

Due to the high stiffness of the dynamical system and the strong magnetic force generated by the magnet, the vibrating mass is firmly held in place and, when it moves, it does so with intense vibrations at high speeds. Fig. 5 illustrates the velocity of the vibrating mass along with the actual desired velocity and the filtered desired velocity in two trajectory tracking scenarios: (a) piecewise step and (b) harmonic trajectory. As shown in Fig. 5-a, the desired velocity for the piecewise step trajectory is zero at all points except for the discontinuous points, where it experiences a sudden increase. During these jumps, the velocity of the vibrating mass can be observed to oscillate with an almost constant amplitude. In Fig. 5-b, for the harmonic trajectory tracking scenario, the harmonic velocity of the desired trajectory, along with the filtered values, are plotted. The velocity of the vibrating mass exhibits much larger oscillations around the desired velocity in this scenario. The presence of significant oscillations in the system's velocity indicates the stability and effectiveness of the control algorithm, which has successfully managed to control this high-stiffness dynamical system, forcing it to track the desired trajectory effectively.

Considering the dependence of coil current magnitude on the position of the vibrating mass, it can be observed in Fig. 6 that the current behavior closely resembles the motion of the mass in trajectory tracking. As shown in Fig. 6-a, during the piecewise step trajectory tracking, the coil generates a current with a magnitude of less than a few milliamperes, exhibiting behavior similar to the piecewise step trajectory. In Fig. 6-b, the current generated in the coil for the harmonic trajectory tracking scenario is depicted, which, in comparison to the previous scenario, has a smaller magnitude and follows the harmonic behavior of the desired trajectory in the second scenario as well.

The control input applied to the second-order actuator dynamics is depicted in Fig. 7. Due to the use of a small time step, the control input exhibits pronounced oscillations, and not all data points are detailed in the figure. Therefore, in Fig. 7, the applied control input is illustrated for the first 0.1 seconds. As shown in Fig. 7-a, the control input in the piecewise step

trajectory tracking scenario is presented, with values staying within the actuator's saturation limits along the entire trajectory. It is important to note that no external saturation function is utilized for this control system, and the controller ensures adherence to the saturation limits by filtering the desired values. Fig. 7-b displays the control input computed by the control algorithm in the harmonic trajectory tracking scenario, where the input remains within the actuator's saturation limits throughout the tracking operation.

As indicated in the derived equations, by calculating and applying the control input, the appropriate actuation voltage is applied to the coil, and by generating current in the coil, flux is created in the left and right branches of the iron yoke. Fig. 8 illustrates the generated fluxes in the left and right halves of the iron yoke over time. As observed in Fig. 8-a, during the piecewise step trajectory tracking, the flux in the left and right halves of the iron yoke is produced on the scale of $10^{-4}Wb$ and exhibits behavior similar to the current produced in the coil. It can also be seen that the generated fluxes in the two parts of the iron yoke are symmetrically drawn relative to a horizontal line with a negative value, indicating their interdependence and lack of independence from each other. Fig. 8-b depicts the fluxes generated in the two left and right parts of the iron yoke, which are proportionate to the harmonic current produced in the coil and exhibit harmonic behavior, being dependent on each other. An important point to note here is that although different values of control input have been applied to the system in the two tracking scenarios, the values of current and generated fluxes in both scenarios are close to each other. It can be said that the difference in the calculated control input in the two scenarios is due to the influence of the position and velocity of the vibrating mass on current and flux generation.

Fig. 9 represents the applied electromagnetic force on the dynamic system. By calculating the maximum and minimum values of the electromagnetic force for each of the position and velocity control modes, the control mode-switching mechanism can select the appropriate control mode. As seen in Fig. 9-a, during the piecewise step trajectory tracking, the control input is determined using a lookup table based on the required electromagnetic force for system control, and the actual electromagnetic force is applied to the system. Throughout the trajectory, the calculated values have remained within the range between the maximum and minimum values, indicating the accuracy of the lookup table's performance. Fig. 9-b shows the values of the electromagnetic force resulting from the application of control input, which has not exceeded the calculated ranges at any point. Given the assumed density for the lookup table, it is expected that the electromagnetic force values calculated due to the control input may differ from the expected electromagnetic force values of the control algorithm. Therefore, the difference between these electromagnetic force values is plotted in the following graph.

Fig. 10 illustrates the electromagnetic force in both the piecewise step trajectory tracking and harmonic trajectory tracking scenarios. As depicted in Fig. 10-a, the electromagnetic force applied to the dynamic system, along with the values computed by the control algorithm during piecewise step trajectory tracking, is shown. Despite significant variations in the calculated electromagnetic force by the controller, the utilization of a lookup table and considering slow dynamics for the actuator have resulted in the smooth and continuous application of electromagnetic force to the dynamics. The electromagnetic force computed by the controller, along with the applied values to the dynamics after applying the control input in the harmonic trajectory tracking scenario, is also presented in Fig. 10-b. Similar to the piecewise step trajectory tracking scenario, in this scenario, the applied electromagnetic force to the dynamics has been smooth and effectively attenuated oscillations with a high-frequency controller.

The stability coefficients of the position control mode and velocity control mode during the tracking operation, which were within the stability range, are visible in Fig. 11. As shown in Fig. 11-a, the stability coefficients for the position control mode and velocity control mode, along with their normal probability density function (PDF) distributions, are plotted in the first scenario. Examining the normal PDF of each control mode reveals that the stability coefficients for the position control mode are closer to 1. This implies that the position error variable has smoothly and consistently decreased in magnitude. Additionally, for the velocity control mode, the stability coefficients have exhibited almost a normal distribution, and by placing more coefficients closer to zero, more control energy has been utilized for velocity control. Fig. 11-b illustrates the stability coefficients calculated for the harmonic trajectory tracking scenario. The distribution of stability coefficients in this scenario is similar to the previous one, with the position control mode utilizing less control energy compared to the velocity control mode.

To investigate the active control mode at each moment, Fig. 12 can be examined. As seen in Fig. 12-a, the active control mode is indicated with different colors during the piecewise step trajectory tracking. It is evident that the control mode

predominantly favors the velocity control mode, and during the jumps, the dominant control mode is the position control mode. Fig. 12-b depicts the active control mode at each moment in the harmonic trajectory tracking scenario. Based on Fig. 12-b, it can be stated that the active control mode has switched relatively uniformly between the two position and velocity control modes.

During system simulation, it is crucial to select simulation parameters correctly, including the simulation time step size and the natural frequency of the actuation system. As seen in Fig. 13-a, the performance of the control system is compared for different time step values. The optimal choice for the time step is $T = 100\mu\sec$, where the control system achieved the least overshoot and oscillations while tracking the desired trajectory. Increasing the time step size led to larger overshoot and oscillations, although the settling time increased with decreasing time step size. Excessive reduction in the time step size caused system instability and increased tracking error. Fig. 13-b illustrates the comparison of the control system's performance for various natural frequency values of the control actuator. Reducing the natural frequency of the actuator resulted in reduced oscillation amplitude and tracking error, with the best performance achieved at $\omega_0 = 2\,Rad/\sec$. Excessively reducing the natural frequency led to system instability, causing the tracking error to deteriorate after the desired trajectory jump.

4. Conclusion

In conclusion, this paper marks a substantial advancement in both the modeling and control algorithm design for electromagnetic systems. The system modeling section introduces pioneering elements, encompassing the incorporation of voltage source equations supplying current to the coil, embracing a comprehensive state-space framework without simplifications, and purposefully avoiding linearization in the proposed control algorithm. The control algorithm exhibits a plethora of noteworthy features, such as the integration of nonlinear electromagnetic equations, achieving nanometer-level precision control despite constraints and second-order dynamics, implementing a trajectory filtering mechanism, utilizing an adaptive lookup table, computing electromagnetic force for both control modes, employing switchable control modes, and introducing a tuning parameter for controller behavior adjustment. Collectively, these features empower precise control of the electromagnetic system, showcasing suitability for applications demanding high-precision control amidst system limitations and varying constraints. The research's initial phase involved extracting open-loop equations, capturing the dynamic aspects of voltage sources, nonlinearity from position and velocity functions in the control input, and intricate characteristics of electromagnetic force. Developed within a comprehensive state-space framework, unburdened by simplifications or reliance on equilibrium point linearization, these equations laid the foundation for a sophisticated two-mode control algorithm. Rooted in stable reaching laws for position and velocity control modes, this algorithm facilitated precise trajectory tracking without the need for linearization around equilibrium points, a departure from conventional approaches. The study systematically addressed inherent constraints within the actuation system, incorporating saturation limitations on electromagnetic force into the control algorithm as effective filters for desired trajectory values, enhancing the control system's resilience and reliability. To enhance adaptability and real-time decision-making, an adaptive one-step cost function was integrated into the switching control mode mechanism, dynamically determining the optimal control mode and enhancing the system's agility. The inclusion of a weighting parameter in the cost function allowed fine-tuning of the control system's behavior to meet specific application demands. Ensuring continuous precision, an adaptive look-up table was employed, continually updated to map control inputs to electromagnetic force, facilitating the calculation of highly precise trajectory tracking control inputs tailored to the evolving system dynamics.

Conflict of Interest: This manuscript includes no potential conflict of interest.

Data Usage: This study does not dependent upon any copy-right supported data.

Funding Information: This study received no funding.

References

1. Hoang, M. C., Liu, S., Nguyen, K. T., et al., “DEMA: robotic dual-electromagnet actuation system integrated with localization for a magnetic capsule endoscope”, *Sensors Actuators A Phys.*, **361**, p. 114596 (2023).

https:// doi.org /10.1016/j.sna.2023.114596.

2. Deng, S., Cheng, X., Wu, H., et al., "Multi-objective optimization configuration of redundant electromagnetic actuators in fault-tolerant control of active magnetic bearing system", *ISA Trans.*, **140**, pp. 293–308 (2023).

https:// doi.org /10.1016/j.isatra.2023.06.015

3. Ru, C., Liu, X., and Sun, Y., *Nanopositioning technologies fundamentals and applications,* Springer*,* Switzerland (2016).

https:// doi.org /10.1007/978-3-319-23853-1

4. Stadler, G., Csencsics, E., Ito, S., et al., "High precision hybrid reluctance actuator with integrated orientation independent zero power gravity compensation", *IEEE Trans. Ind. Electron.*, **69**(12), pp. 13296–13304 (2022).

https:// doi.org /10.1109/TIE.2021.3137444

5. Takahashi, K., Makino, R., and Ito, S., "Sample-tracking vibration isolation with rigid negative stiffness for broad bandwidth", *Mechatronics*, **99**, p. 103159 (2024).

https:// doi.org /10.1016/j.mechatronics.2024.103159

6. Liao, S., "A hybrid electromagnetic-piezoelectric actuated tri-axial fast tool servo integrated with a three-dimensional elliptical vibration generator", *Econ. Lett.*, p. 111045 (2023).

https:// doi.org /10.1016/j.precisioneng.2023.12.006

7. Fadaie, M., Abbaszadeh, K., and Siadatan, A., "Fast response predictive controllers for mono-inverter dual parallel permanent magnet synchronous", *Sci. Iran.*, (2023).

https:// doi.org /10.24200/sci.2023.61180.7185

8. Huang, W., Zhu, Z., Zhang, X., et al., "A hybrid electromagnetic-piezoelectric actuated tri-axial fast tool servo integrated with a three-dimensional elliptical vibration generator", *Precis. Eng.*, **86**, pp. 213–224 (2024).

https:// doi.org /10.1016/j.precisioneng.2023.12.006

9. Yu, B., Wang, X., Member, G. S., et al., "Electromagnetic-mechanical modeling and evaluation of a 2-DoF parallel-kinematic compliant nano-positioning stage based on normal-stressed electromagnetic actuators", *IEEE Trans. Autom. Sci. Eng ,* pp. 1-14 (2024).

https:// doi.org /10.1109/TASE.2024.3354943

10. Lázaro, R. P. S., Fuentes-Aguilar, R., and Chairez, I., "Trajectory tracking control with state restricted gains for a magnetic pendulum using electromagnetic actuators", *ISA Trans.*, **139**, pp. 475–483 (2023).

https:// doi.org /10.1016/j.isatra.2023.03.036

11. Huang, W. W., Li, L., Zhu, Z., et al., "Modeling, design and control of normal-stressed electromagnetic actuated fast tool servos", *Mech. Syst. Signal Process.*, **178**, p. 109304 (2022).

https:// doi.org /10.1016/j.ymssp.2022.109304

12. Kastor, N., Dandu, B., Bassari, V., et al., "Ferrofluid electromagnetic actuators for high-fidelity haptic feedback", *Sensors Actuators A Phys.*, **355**, p. 114252 (2023).

https:// doi.org /10.1016/j.sna.2023.114252

13. Wu, D., Xie, X., and Zhou, S., “Design of a normal stress electromagnetic fast linear actuator”, *IEEE Trans. Magn.*, **46**(4), pp. 1007–1014 (2010).

https:// doi.org /10.1109/TMAG.2009.2036606

14. Wang, X., Meng, Y., Huang, W. W., et al., “Design, modeling, and test of a normal-stressed electromagnetic actuated compliant nano-positioning stage”, *Mech. Syst. Signal Process.*, **185** (2023).

https:// doi.org /10.1016/j.ymssp.2022.109753

15. Arand, S. J. and Fard, J. R., “Sensorless position control of an axial flux-switching permanent-magnet motor based on high-frequency pulsating voltage vector injection”, *Sci. Iran.*, **30**(3), pp. 1097–1105 (2023).

https:// doi.org /10.24200/sci.2021.57434.5239

16. Ştefănescu, D. M., “Handbook of force transducers - principles and components”, Springer, Berlin (2011).

https:// doi.org /10.1007/978-3-642-18296-9

17. Helwig, N. E., Hong, S., and Hsiao-wecksler, E. T., *The design of high performance mechatronics high-tech functionality by multidisciplinary system integration*, IOS, Amsterdam (2020).

https:// doi.org /10.3233/STAL9781643680514

18. Ito, S., Troppmair, S., Lindner, B., et al., “Long-range fast nanopositioner using nonlinearities of hybrid reluctance actuator for energy efficiency”, *IEEE Trans. Ind. Electron.*, **66**(4), pp. 3051 - 3059 (2019).

https:// doi.org /10.1109/TIE.2018.2842735

19. Ito, S., Lindner, B., and Schitter, G., “Sample-tracking vibration isolation with hybrid reluctance actuators for inline metrology”, *IFAC-PapersOnLine*, **52**(15), pp. 537–542 (2019).

https:// doi.org /10.1016/j.ifacol.2019.11.731

20. Cigarini, F., Ito, S., Troppmair, S., et al., “Comparative finite element analysis of a voice coil actuator and a hybrid reluctance actuator”, *IEEJ J. Ind. Appl.*, **8**(2), pp. 192–199 (2019).

https:// doi.org /10.1541/ieejjia.8.192

21. Su, X., Yang, X., and Xu, Y., “Analytical modelling of a hybrid reluctance motor based on magnetic equivalent circuit”, *Proc. IEEE Int. Conf. Ind. Technol.* (2023).

https:// doi.org /10.1109/ICIT58465.2023.10143108

22. Kluk, D. J., Boulet, M. T., and Trumper, D. L., “A high-bandwidth, high-precision, two-axis steering mirror with moving iron actuator”, *Mechatronics*, **22**(3), pp. 257–270 (2012).

https:// doi.org /10.1016/j.mechatronics.2012.01.008

23. Ramirez-Laboreo, E., Roes, M. G. L., and Sagues, C., “Hybrid dynamical model for reluctance actuators including saturation, hysteresis, and Eddy currents”, *IEEE/ASME Trans. Mechatronics*, **24**(3), pp. 1396–1406 (2019).

https:// doi.org /10.1109/TMECH.2019.2906755

24. Cigarini, F., Csencsics, E., Schlarp, J., et al., “Multiphysics finite element model for the computation of the electro-mechanical dynamics of a hybrid reluctance actuator”, *Math. Comput. Model. Dyn. Syst.*, **26**(4), pp. 322–343 (2020).

https:// doi.org /10.1080/13873954.2020.1766509

25. Kowsari Mogadam, S., Salimi, M., Bathaee, S. M. T., et al., "A novel Lyapunov-based nonlinear controller design for model-based MPPT of the thermoelectric generators", *Sci. Iran.*, (2023).

https:// doi.org /10.24200/sci.2023.61170.7177

26. Burgstaller, I., Ito, S., Fujimoto, H., et al., "Development of reluctance actuator for high-precision positioning and scanning motion", *2021 IEEE Int. Conf. Mechatronics, ICM 2021* (2021).

https:// doi.org /10.1109/ICM46511.2021.9385649

27. Csencsics, E., Schlarp, J., and Schitter, G., "Bandwidth extension of hybrid-reluctance-force-based tip/tilt system by reduction of eddy currents", *IEEE/ASME Int. Conf. Adv. Intell. Mechatronics, AIM*, pp. 1167–1172 (2017).

https:// doi.org /10.1109/AIM.2017.8014176

28. Ariba, Y., "singular singular perturbation perturbation approach approach for for the the singular perturbation approach for the singular perturbation approach for the control of electromagnetic actuators singular perturbation approach for the control of electromagne", *IFAC,* **56**, pp. 6057-6062 (2023).

https:// doi.org /10.1016/j.ifacol.2023.10.661

29. Asrari, H., Mohammadzaman, I., and Allahverdizadeh, F., "Robust state-feedback controller for linear parameter-varying systems with time-invariant uncertainties", *Sci. Iran.*, **30**(3), pp. 1148–1157 (2023).

https:// doi.org /10.24200/sci.2021.56871.4953

30. Andrada, P., Blanqué, B., Martinez, E., et al., "New linear hybrid reluctance actuator", *Proc. - 2014 Int. Conf. Electr. Mach. ICEM 2014*, pp. 585–590 (2014).

https:// doi.org /10.1109/ICELMACH.2014.6960239

31. Ebrahimi, M. and Homaeinezhad, M., "Compensation of friction and stick-slip uncertainties in trajectory tracking control of servo DC machines considering actuation constraints", *SAGE*, **238**(3), pp. 479–503 (2023).

https:// doi.org /10.1177/09596518231196830

32. Homaeinezhad, M. R. and Ebrahimi, M. M., "Tracking control of Newtonian mechanical systems manipulated by hardly constrained parabolic nonlinear actuator", *Int. J. Dyn. Control*, (2023).

https:// doi.org /10.1007/S40435-023-01365-5

33. Homaeinezhad, M. R. and Gavari, M. A., "Tracking control of nonlinear systems actuated by saturated oscillatory force generator", *Eur. J. Control*, **75**, p. 100891 (2024).

https:// doi.org /10.1016/j.ejcon.2023.100891

34. Homaeinezhad, M. R. and Abbasi Gavari, M., " Feedback control of actuation-constrained moving structure carrying Timoshenko beam ", *Int. J. Robust Nonlinear Control*, **33**, pp. 1785–1806 (May) (2022).

https:// doi.org /10.1002/rnc.6471

Figures and Tables Captions

Figure 1. Schematic representation of the proposed control algorithm for the nonlinear vibratory mass system with an electromagnetic actuator.

Figure 2. (a) Diagram of the magnetic dynamic system, comprising a fixed-piece iron yoke, control coil, powerful permanent magnet, vibrating mass, and nonlinear stiffness damping applied to mass M. (b) The equivalent electromagnetic circuit of the system includes electrical components substituted for mechanical and magnetic components

Figure 3. Plots of magnetic fluxes in the left and right branches of the iron core, coil current, and electromagnetic force for various values of the position and velocity of the vibrating mass

Figure 4. Controlled position of mass M along with actual desired trajectory and filtered desired trajectory in the tracking scenario (a) piecewise step and (b) harmonic

Figure 5. The velocity of mass M along with the actual desired velocity and the filtered desired velocity in the tracking scenarios of (a) piecewise step and (b) harmonic trajectory

Figure 6. The computed current magnitude due to the application of voltage to the system equations in the (a) piecewise step trajectory tracking scenario and (b) harmonic trajectory tracking scenario

Figure 7. The control input computed by the control algorithm in scenarios (a) piecewise step trajectory tracking and (b) harmonic trajectory tracking

Figure 8. Fluxes generated in the left and right halves of the iron yoke due to the application of control input and current production in the branches in scenarios (a) piecewise step trajectory tracking and (b) harmonic trajectory tracking

Figure 9. The applied electromagnetic force on mass M, calculated between its maximum and minimum values, and applied to the system in scenario (a) piecewise step trajectory tracking and (b) harmonic trajectory tracking

Figure 10. The electromagnetic force applied to mass M, calculated within its maximum and minimum bounds, has been exerted on the system in scenarios (a) piecewise step trajectory tracking and (b) harmonic trajectory tracking

Figure 11. Stability coefficients of position control mode and velocity control mode with normal PDF plots in the (a) piecewise step trajectory tracking and (b) harmonic trajectory tracking scenarios

Figure 12. The active control mode determined by control mode switching mechanism in scenarios (a) piecewise step trajectory tracking and (b) harmonic trajectory tracking

Figure 13. Performance comparison chart of the control system for various simulation parameters in (a) time steps $T = 40$, $T = 50$, $T = 100$, $T = 200$, $T = 300\mu\sec$ and (b) natural frequencies $\omega_0 = 1$, $\omega_0 = 2$, $\omega_0 = 3$, $\omega_0 = 4$, $\omega_0 = 5 Rad/\sec$ for the control actuator during the tracking operation

Table 1. Simulation parameters used in the paper along with descriptions

Table 2. Desired trajectories considered for two tracking scenarios along with controller tuning parameters in the respective scenario

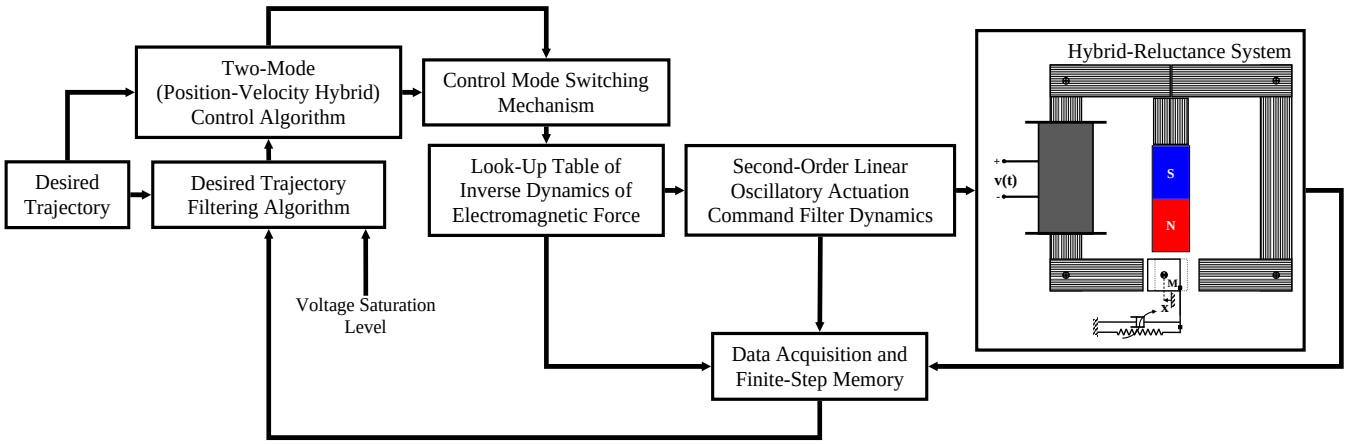

Figure 1

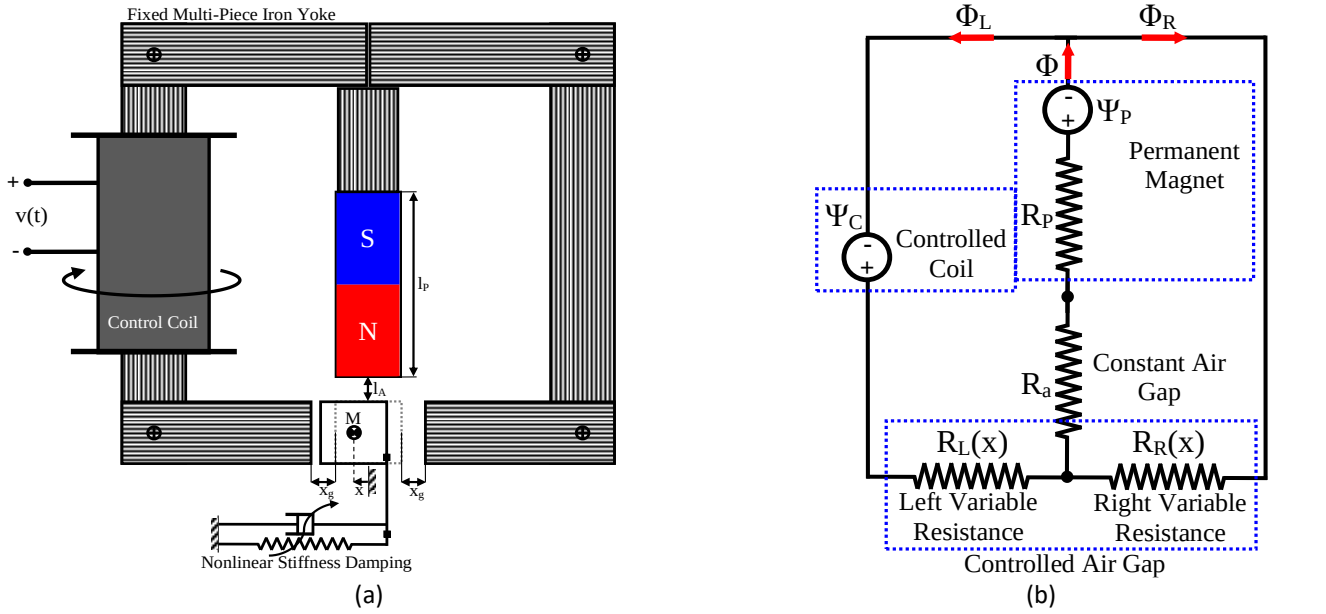

Figure 2

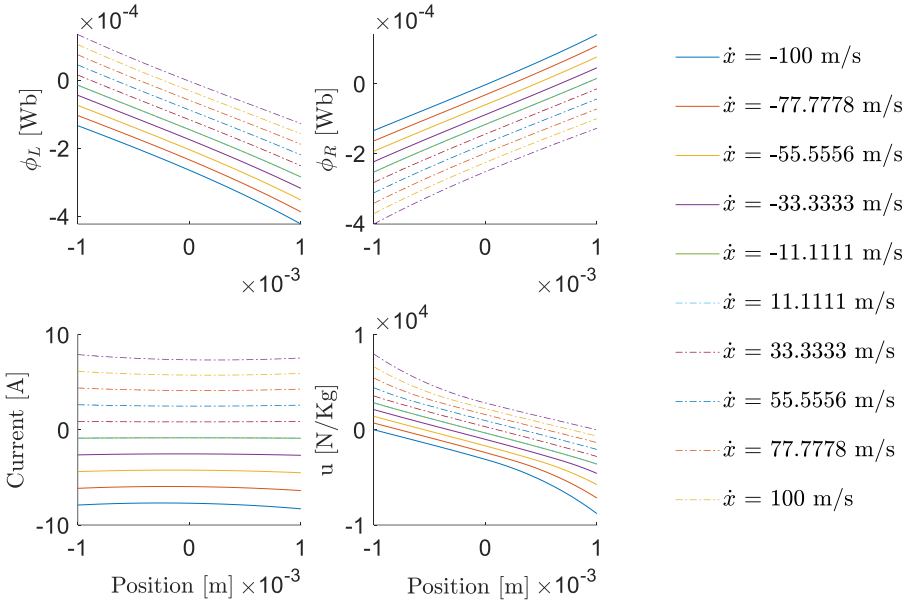

Figure 3

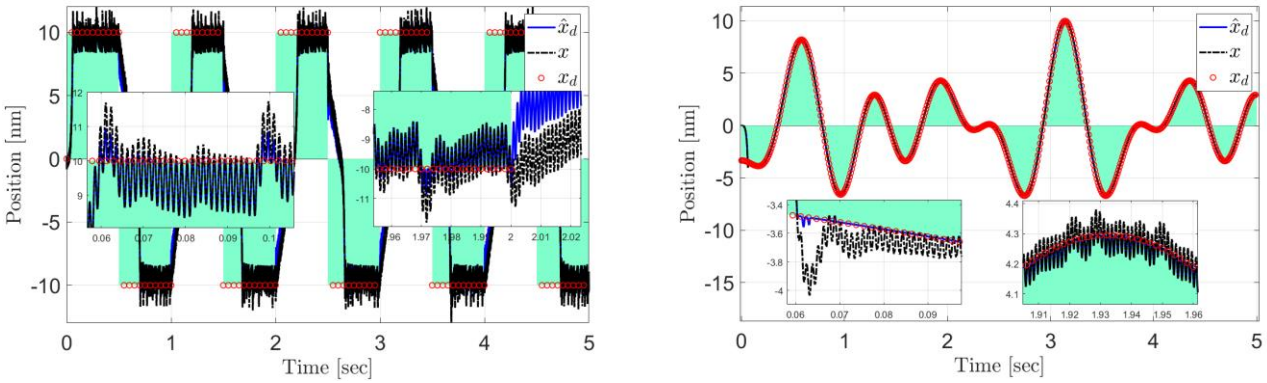

(a) (b)

Figure 4

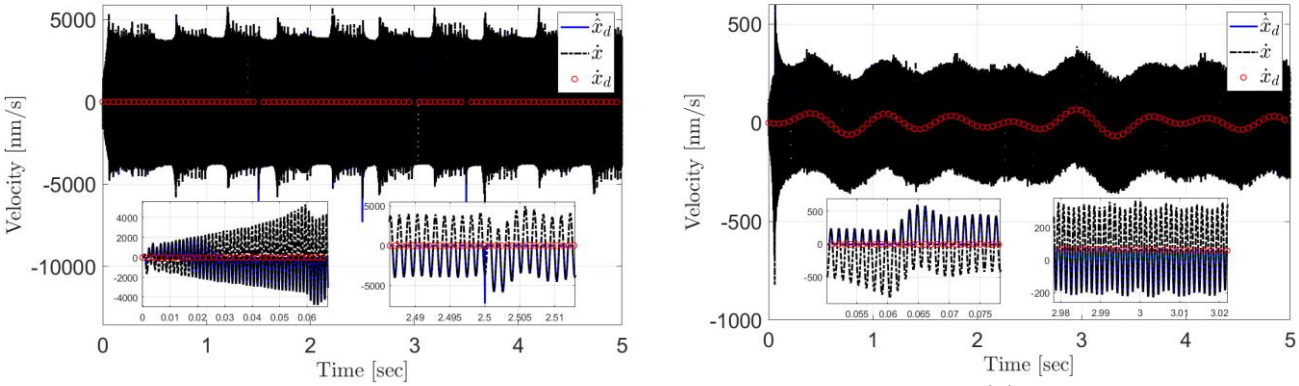

(a) (b)

Figure 5

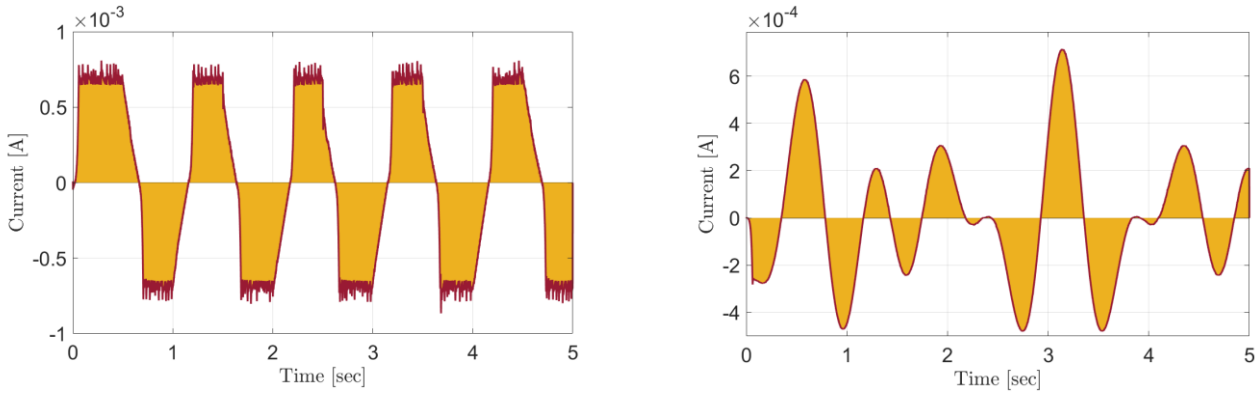

(a) (b)

Figure 6

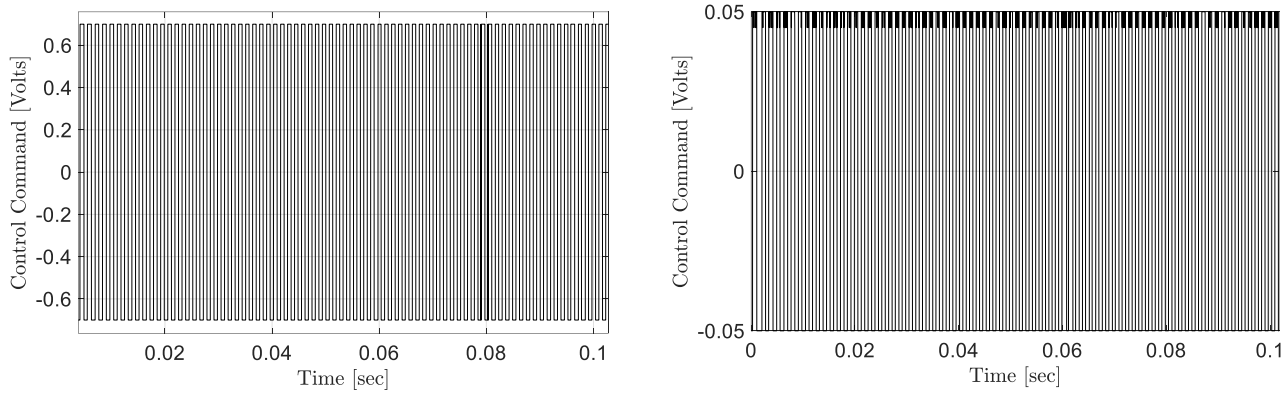

(a) (b)

Figure 7

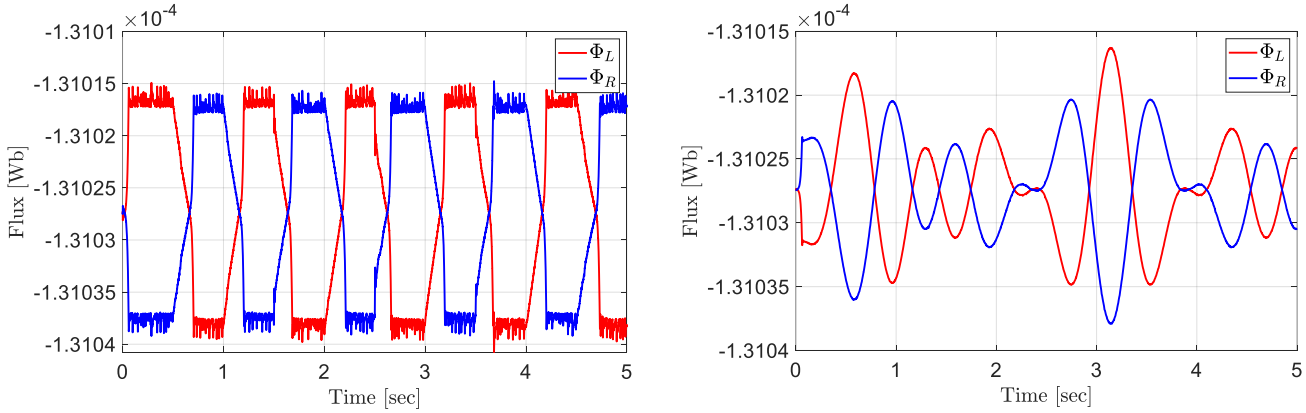

(a) (b)

Figure 8

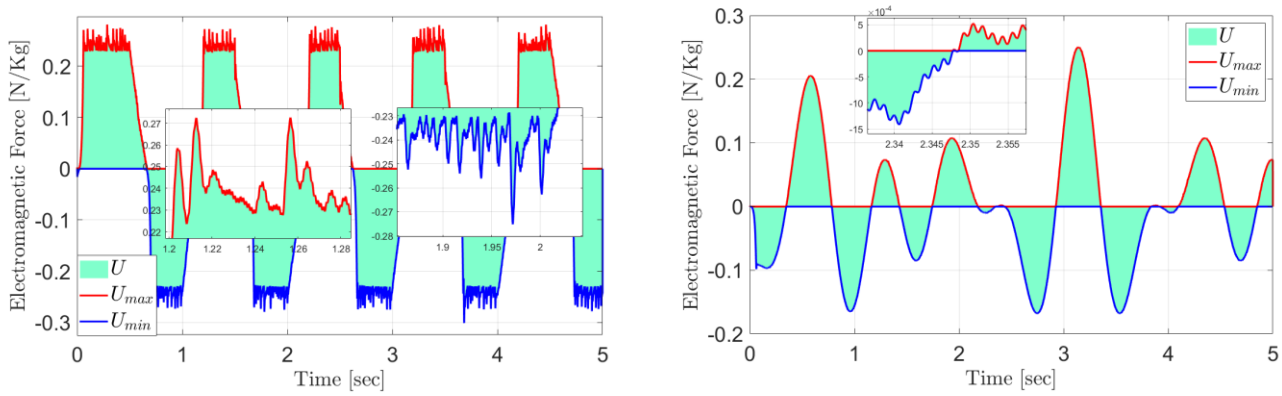

(a) (b)

Figure 9

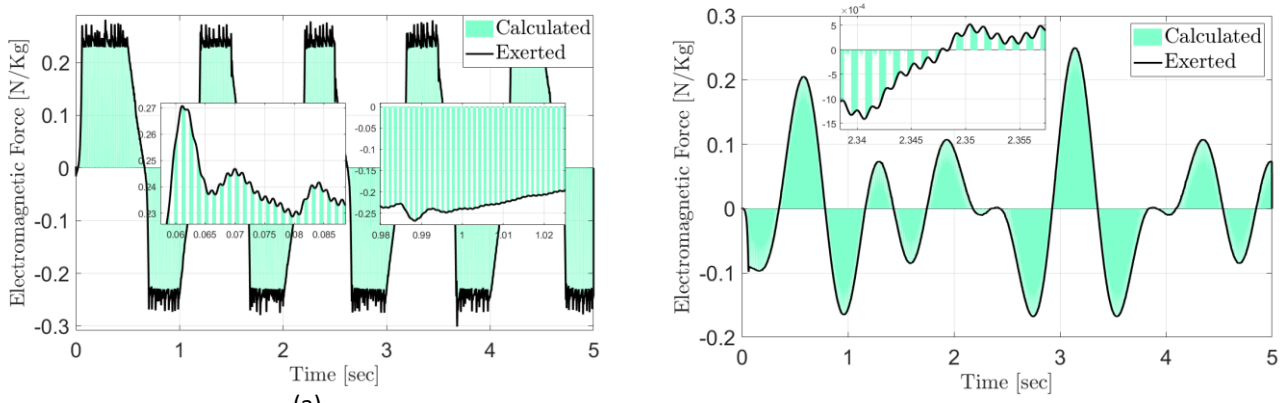

(a) (b)

Figure 10

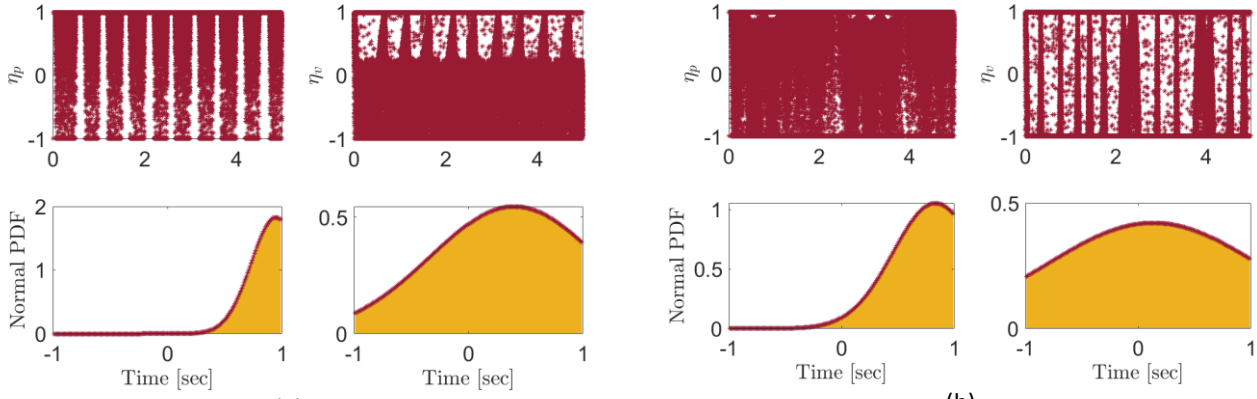

(a) (b)

Figure 11

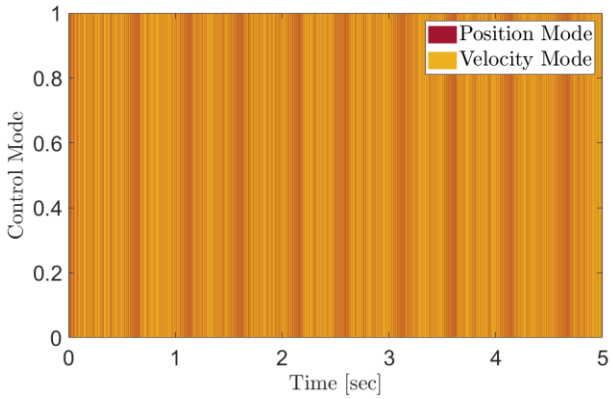

(a)

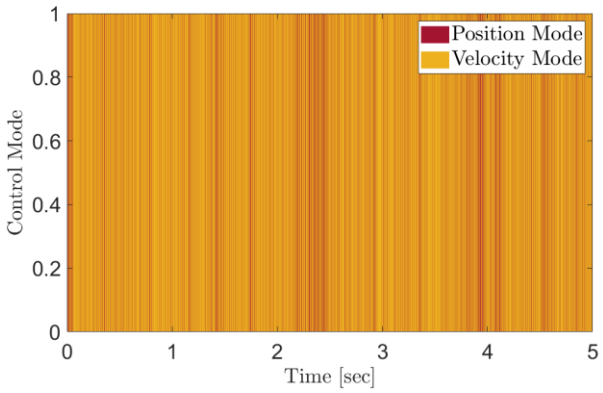

(b)

Figure 12

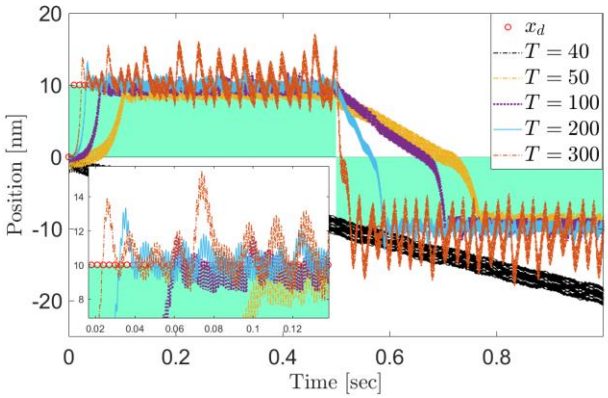

(a)

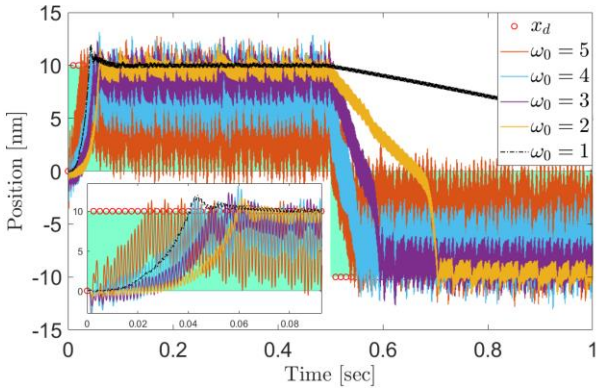

(b)

Figure 13

Table 1

Simulation Parameter	Value	Explanation	Simulation Parameter	Value	Explanation
μ_0	$4\pi\times10^{-7}[Wb/A.m]$	Air Permeability	M	$0.04[kg]$	Mass
N_L	120	Coil Turns	c_0	$4[N.\sec/m]$	Linear Damping Coeff.
l_P	$19[mm]$	Length of Iron Core	k_0	$1000000[N/m]$	Linear Spring Coeff.
l_A	$1[mm]$	Distance of Mass from Iron Core	k_1	$100[N/m^3]$	Nonlinear Spring Coeff.
x_g	$1[mm]$	Gap Distance of Mass	c_1	$1[N.\sec^2/m^2]$	Nonlinear Damping Coeff.
A	$225\times10^{-6}[m^2]$	Magnetic Flux Area	T	$0.00001[\sec]$	Time Step Size
R	$0.7[\Omega]$	Coil Resistance	ω_0	$2[Rad/\sec]$	Actuator Natural Frequency
M_0	$10^6[N/Wb]$	Magnetic Field Strength	ξ	0.2	Actuator Damping Ratio

.

Table 2

Scenario Parameter	piece wise step	harmonic
$x_d[nm]$	$sign(2\pi t)$	$\frac{1}{3}[-\cos(5t)-\cos(7t)+\cos(10t)]$
$v_0[volts]$	0.7	0.05
W_{pv}	0.3	0.95

Biography

Mohammad Reza Homaeinezhad received his B.Sc. degree in mechanical engineering from K.N. Toosi University of Technology, Tehran, Iran, 2003. He received his M.Sc. degree in dynamics and control from the Department of Mechanical Engineering, K.N. Toosi University of Technology, Tehran, Iran, 2005. He completed his PhD degree in dynamics and control from K.N. Toosi University of Technology, Tehran, Iran, 2010. He is currently serving as a Professor at the Department of Mechanical Engineering, K.N. Toosi University of Technology, Tehran, Iran. His research interests mainly include Advanced Mechatronics, Feedback Controllers, Artificial Intelligence, etc.

Mohammad Moeen Ebrahimi received his B.Sc. degree in mechanical engineering from K.N. Toosi University of Technology, Tehran, Iran, 2021. He received his M.Sc. degree in dynamics and control from the Department of Mechanical Engineering, K.N. Toosi University of Technology, Tehran, Iran, 2024. His research interests mainly include Nonlinear Control Systems, Swarm Control, Advanced Mechatronics, etc.

Mohammad Mousavi Alvar received his B.Sc. degree in mechanical engineering from K.N. Toosi University of Technology, Tehran, Iran, 2022. He is student in M.Sc. degree in dynamics and control from the Department of Mechanical Engineering,

K.N. Toosi University of Technology, Tehran, Iran. His research interests mainly include Nonlinear Control Systems, Electromagnetic Actuators, etc.